Research in Astron. Astrophys. **2010** Vol. **10** No. **3**, 220–226
http://www.raa-journal.org *http://www.iop.org/journals/raa*

***R**esearch in*
***A**stronomy and*
***A**strophysics*

Clumpy metal concentrations in elliptical galaxies NGC 4374 and NGC 4636 *

Hai-Guang Xu[1], Jun-Hua Gu[1], Li-Yi Gu[1], Zhong-Li Zhang[2], Yu Wang[1] and Tao An[3]

[1] Department of Physics, Shanghai Jiao Tong University, Shanghai 200240, China; *hgxu@sjtu.edu.cn*
[2] Max-Planck Institut für Astrophysik, D-85740 Garching, Germany
[3] Shanghai Astronomical Observatory, Chinese Academy of Sciences, Shanghai 200030, China

Received 2009 July 28; accepted 2009 December 17

Abstract We present a high spatial resolution study of metal distributions in the nearby, gas-rich elliptical galaxies NGC 4374 and NGC 4636 with the *Chandra* ACIS archive data. We define the hardness ratio $\mathrm{HR}_{\mathrm{FeL}}$ as the ratio of the emission in 0.65–1.4 keV to that in 0.3–0.6 keV and 1.4–3.5 keV (after the magnesium and silicon lines are excluded), and $\mathrm{HR}_{\mathrm{cont}}$ as the ratio of the emission in 1.4–3.5 keV to that in 0.3–0.6 keV, so that the $\mathrm{HR}_{\mathrm{FeL}}$ and $\mathrm{HR}_{\mathrm{cont}}$ maps can be used to trace the iron abundance and gas temperature distributions, respectively. By applying the à Trous wavelet algorithm to the obtained emission hardness ratio maps, we reveal that the $\mathrm{HR}_{\mathrm{FeL}}$ distributions are highly irregular, exhibiting strong spatial variations on 0.1–$1R_{\mathrm{e}}$ scales, which do not follow the $\mathrm{HR}_{\mathrm{cont}}$ distributions. Since the effect of temperature variation is small, we conclude that most of the high-$\mathrm{HR}_{\mathrm{FeL}}$ regions are very likely to possess higher abundances than the ambient gas. We also find that these high-$\mathrm{HR}_{\mathrm{FeL}}$ substructures are not associated with either the LMXB or globular cluster populations, thus their origins should be related to AGN activity or mergers.

Key words: galaxies: elliptical and lenticular, cD — galaxies: individual (NGC 4374, NGC 4636) — galaxies: ISM — ISM: abundances — X-rays: galaxies

1 INTRODUCTION

X-ray measurements of metal distributions in the interstellar medium (ISM) of early-type galaxies provide us with robust constraints on the thermal, chemical, and dynamical evolution histories of these galaxies (e.g., Gibson et al. 2007). They also help researchers understand the processes in which metals were synthesized and diffused into the ambient hot plasma of galaxy groups and clusters.

In the era of *ASCA*, iron abundance gradients were revealed unambiguously for the first time within the central ~ 100 kpc in the intra-cluster medium (ICM) of some luminous, relaxed galaxy clusters, which usually host a cD galaxy at the bottom of the gravitational potential well (Makishima et al. 2001 and references therein). In recent years, 2-dimensional mappings of the distributions of both metal abundance and emission hardness ratio with the high-quality *Chandra* data showed, the

* Supported by the National Natural Science Foundation of China.

existence of particular off-center, asymmetric metal concentrations in a few clusters either on cluster scales ($\sim 100\,\mathrm{kpc}$) or on smaller scales ($\sim 10\,\mathrm{kpc}$) (Abell 2199; Johnstone et al. 2002; AWM 7, Furusho et al. 2003; Abell 1060; Hayakawa et al. 2004, 2006; the NGC 507 Group, Kraft et al. 2004; the Perseus Cluster, Sanders et al. 2005; the HCG 62 Group, Gu et al. 2007). In the Perseus Cluster, a high-abundance shell is detected at the edge of a radio mini-halo with two H_α filaments pointing towards it, and was interpreted in terms of AGN activity. In the NGC 507 Group, an arc-like sharp edge aligned with a low-surface brightness radio lobe is detected on the X-ray image, which was ascribed to the excess emission from the high-abundance materials lifted from the group center. In other clusters that exhibit distinct 2-dimensional metal substructures, however, the origins of these substructures are still unclear.

In *Chandra* and *XMM-Newton* studies of some elliptical galaxies (e.g., Ohto et al. 2003; O'Sullivan & Ponman 2004; Randall et al. 2004, 2006), it has been found that the radial iron abundance distributions exhibit complex patterns, implying that in these less massive systems there may exist off-center metal concentrations as well. For example, in the luminous elliptical galaxy NGC 4636, a central iron abundance dip similar to those seen in more massive systems and 2-dimensional metal abundance gradients were reported by Jones et al. (2002) and O'Sullivan et al. (2005), respectively.

In this work, by applying the à Trous wavelet algorithm to measured *Chandra* emission hardness ratio maps, we present a study of 2-dimensional metal distributions in the nearby early-type galaxies NGC 4374 (M84, E1) and NGC 4636 (E0), which are both gas-rich, bright ($L_\mathrm{X} \gtrsim 10^{40}$ erg s^{-1}) members of the Virgo Cluster (Table 1). On the images extracted from the Digitized Sky Survey (DSS) archive and from the Two Micron Sky Survey (2MASS) archive, the two galaxies exhibit no significant or apparent irregularities on galactic scales, although minor structures were reported in previous works, such as dust lanes in the core regions of NGC 4374, and possibly in NGC 4636 (E0) (Xilouris et al. 2004; Carollo et al. 1997; Ravindranath et al. 2001). We calculated the distances to these galaxies by using the distance moduli obtained in the infrared surface brightness fluctuation analysis (Tonry et al. 2001). Throughout the paper, we quote errors at the 90% confidence level unless mentioned otherwise. We adopt the solar abundance standards of Grevesse & Sauval (1998), where the iron abundance relative to hydrogen is 3.16×10^{-5} in number. We employ the cosmological parameters $H_0 = 70\,\mathrm{km\,s^{-1}}$ Mpc^{-1}, $\Omega_m = 0.3$, and $\Omega_\Lambda = 0.7$.

Table 1 Basic Properties of the Targets[a]

Name	RA (h m s; J2000)	Dec (d m s; J2000)	z	N_H (10^{20} cm^{-2})	Distance (Mpc)	R_e (arcmin kpc^{-1})	L_B ($10^{10} L_{\mathrm{B}\odot}$)	L_R ($10^{10} L_{\mathrm{R}\odot}$)	Type
NGC 4374	12 25 03.74	+12 53 13.1	0.00354	2.60	$18.36^{+0.95}_{-0.91}$	0.910/4.9 $\pm$ 0.3	4.84 ± 0.22	7.05 ± 0.32	E1
NGC 4636	12 42 49.87	+02 41 16.0	0.00313	1.81	$14.66^{+0.90}_{-0.85}$	1.694/7.2 $\pm$ 0.4	2.25 ± 0.21	3.88 ± 0.36	E0

[a] From left to right, the columns give the target names (Col. 1), RA and Dec in J2000 (Cols. 2–3), redshifts (Col. 4), Galactic absorptions (Col. 5; Dickey & Lockman 1990), distances calculated from the measurements of infrared surface brightness fluctuations (Col. 6; Tonry et al. 2001), effective radii (Col. 7; Faber et al. 1989), B- and R-band luminosities (Cols. $8-9$; de Vaucouleurs et al. 1991; Prugniel & Simien 1996), and types (Col. 10).

2 OBSERVATION AND DATA REDUCTION

NGC 4374 and NGC 4636 were observed with the *Chandra* ACIS instrument in VFAINT mode on 2000 May 19 for 30.6 ks (ObsID 803) and in FAINT mode on 2000 January 26 for 54.9 ks (ObsID 323), respectively. The centers of the target galaxies were positioned on the ACIS S3 chip (CCD 7) with a small offset from the nominal pointing for the S3 chip, so that most of the X-ray halos are covered by the S3 chip. We applied the CIAO 3.4 software and the newest calibration

(CALDB version 4.1.1) to process the Level-1 data acquired from the S3 chip. The CTI correction was executed for the datasets taken at a focal-plane temperature of $-120\,^{\circ}$C (NGC 4374), but not for the datasets taken at -110°C (NGC 4636), for which there is no available CTI calibration. We kept events with *ASCA* grades 0, 2, 3, 4, and 6, and removed bad pixels, bad columns, and columns adjacent to bad columns and node boundaries.

In order to avoid occasional background flares, we examined the light curves extracted from the source-free regions on the backside-illuminated S3 chip, and removed the intervals contaminated by the particle events that raised the count rate to $> 120\%$ of the mean quiescent value. For NGC 4374, the observation was only slightly affected by weak flares, which lasted about 2.1 ks, or about 7% of the total effective exposure ($T_{\rm tot}$). The cumulative flare-contaminated interval for NGC 4636, on the other hand, is 13.4 ks, or 24% of $T_{\rm tot}$.

3 X-RAY ANALYSIS AND RESULTS

The spatial distribution of the diffuse X-ray emission in NGC 4374 (Fig. 1; see also Finoguenov & Jones 2001) shows an H-shaped structure that encloses two X-ray cavities. The cavities coincide with two radio lobes, which connect to two luminous jets straddling the central compact radio core, respectively. In NGC 4636, there exist two apparent arm-like X-ray structures extending towards the northeast and southwest, respectively. Although their origins were associated with the AGN activity (Nagar et al. 2000; Jones et al. 2002; O'Sullivan et al. 2005), the low luminosities and short spatial extensions of their radio counterparts suggest that the possibility of the X-ray arms being formed during a non-AGN process (e.g., a merger event) still cannot be ruled out.

We define the hardness ratio $\mathrm{HR}_{\rm FeL}$ as the ratio of the emission in 0.65–1.4 keV, a significant part of which comes from the blending of Fe-L lines, to the continuum-dominated emission extracted in 0.3–0.6 keV and 1.4–3.5 keV, after the magnesium and silicon lines in 1.4–3.5 keV are excluded. We note that, given the typical abundance range of the ISM, the ratio $\mathrm{HR}_{\rm cont}$, i.e., the emission ratio of the 1.4–3.5 keV continuum to the 0.3–0.6 keV continuum, is not sensitive to variations in metal abundance in 0.5–0.8 keV, the typical temperatures of the ISM, and it varies slowly with abundance in 0.8–1.2 keV. To be specific, when $\mathrm{HR}_{\rm cont}$ is employed to approximate the temperature gradients in the ISM, the typical bias is estimated to be $\lesssim$ 0.03–0.05 keV in 0.5–0.8 keV, and up to about 0.1 keV in 0.8–1.2 keV. Thus, $\mathrm{HR}_{\rm cont}$ can be used as a reliable tool to trace the gas temperature distributions.

After subtracting the backgrounds, which were extracted from the *Chandra* blank fields in the same detector regions as the observation and then properly renormalized, we calculate and plot the 2-dimensional distributions of $\mathrm{HR}_{\rm FeL}$ in Figure 2, which is overlaid with the contours of the hardness ratio $\mathrm{HR}_{\rm cont}$. In calculating both the $\mathrm{HR}_{\rm FeL}$ maps and $\mathrm{HR}_{\rm cont}$ contours, raw count maps are adaptively smoothed with the same Gaussian Kernel ($\sigma = 4''$ and $15''$ for the inner and outer regions, respectively, to ensure that a significance better than 3 per smoothing beam in all bands) by using the CIAO tool csmooth, and then exposure-corrected. We keep all the point sources detected with the CIAO tools celldetect and wavdetect when calculating the hardness ratio maps, which will not significantly affect our analysis that follows. In fact, because the point sources possess totally different spectral properties as compared with the gas component, nearly all the detected point sources appear as tiny dark spots on the $\mathrm{HR}_{\rm FeL}$ maps, showing a hardness ratio that is lower than those of the surrounding regions by a factor of several times. There also exist some unidentified dark spots on the maps, which may be point sources below the detection threshold.

In order to filter insignificant substructures and fake features, many of which are assumed to be caused by the low signal-to-noise ratio, we analyze the observed $\mathrm{HR}_{\rm FeL}$ maps by applying the à Trous wavelet transform algorithm (Shensa 1992). We employ a Gaussian-shaped convolution mask $h(\sigma,l) = e^{-l^2/(2\sigma^2)}/(2\pi\sigma^2)$, and define the corresponding wavelet kernel as $W(l) = h(\sigma,l) - h(2\sigma,l)$, where σ is the scaling parameter. For the $\mathrm{HR}_{\rm FeL}$ map of each galaxy, we perform the convolution of the map and mask to obtain a smooth plane for the scale of $l = 2^1$ pixels. Then,

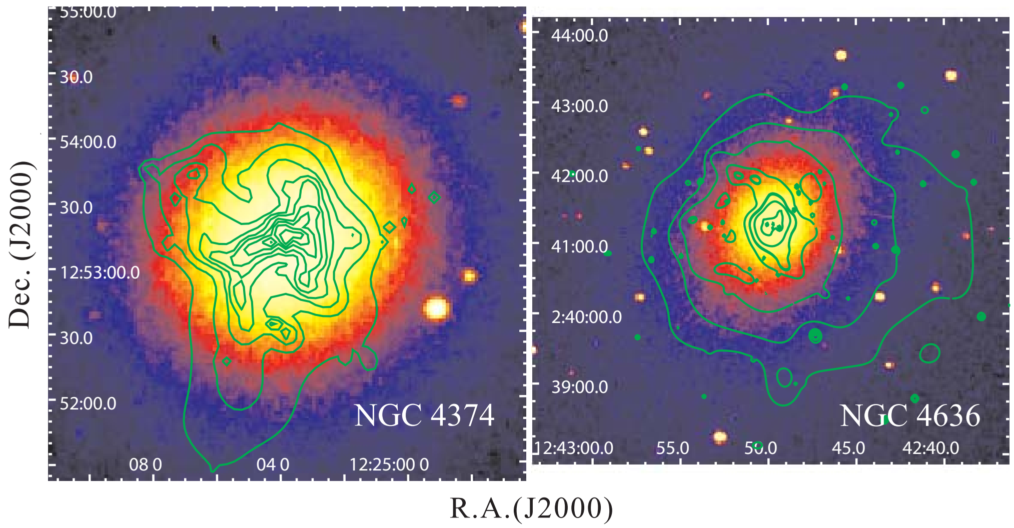

Fig. 1 Optical DSS images of the central $2R_\mathrm{e}$ regions of NGC 4374 and NGC 4636, overlaid with the X-ray intensity contours calculated from the *Chandra* ACIS S3 images (0.7–7 keV) in logarithmic scale in units of photons cm^{-2} s^{-1} pixel^{-2}. The X-ray images have been exposure-corrected, and smoothed by using a minimum significance of 3.

we perform the convolution of the obtained smooth plane and mask to obtain the smooth plane for the next scale ($l = 2^2$ pixels). By repeating this process, a set of eight smooth planes $c_i(x, y)$ ($i = 1,\ 2,\ \ldots,\ 8$) are obtained for scales of $l = 2^n,\ n = 1,\ 2,\ \ldots,\ 8$ pixels, respectively. By calculating the signal difference between any two smooth planes that have adjacent scales, we obtain seven subimages $w_i(x, y) = c_i(x, y) - c_{i+1}(x, y)$. The detection of significant substructures is performed on the subimages with the 4th and 5th scales, which are much larger than the sizes of point sources. To cross check whether or not the point sources have significant affects on the detection, we also have repeated the above detection process by excluding all the identified point sources, and find that the results remain nearly unchanged.

On the other hand, for each galaxy we run 30 repetitions of a Monte-Carlo simulation to simulate its X-ray halo, using the *Chandra* data simulator MARX v4.0 and the imaging and spectral information derived from the observations. For each simulated gas halo, we create a corresponding $\mathrm{HR_{FeL}}$ map, and then decompose the map into seven subimages in the same way as for the observed $\mathrm{HR_{FeL}}$ map. For each galaxy, we examine the statistics of the intensity, size, and shape of the random substructures that appear on the simulated subimages of the 4th and 5th scales, respectively, which are purely caused by the statistical fluctuations. By comparing the observation with the simulations, we identify the intrinsic substructures on the observed $\mathrm{HR_{FeL}}$ maps, whose intensities are beyond the 3σ limit of the local random fluctuations estimated from the Monte-Carlo simulations. The boundaries of these identified substructures are marked with solid grey lines in Figure 3, which shows that in the two galaxies the $\mathrm{HR_{FeL}}$ distribution is highly irregular, exhibiting strong spatial variations. We also mark the regions in which the mean $\mathrm{HR_{FeL}}$ ratio is higher than those of the surrounding regions by a factor of > 2 with dotted black lines.

In general, the distributions of the high-$\mathrm{HR_{FeL}}$ substructures do not follow the $\mathrm{HR_{cont}}$ distributions. This mismatch suggests that the iron abundance distributions may be complex, and many of

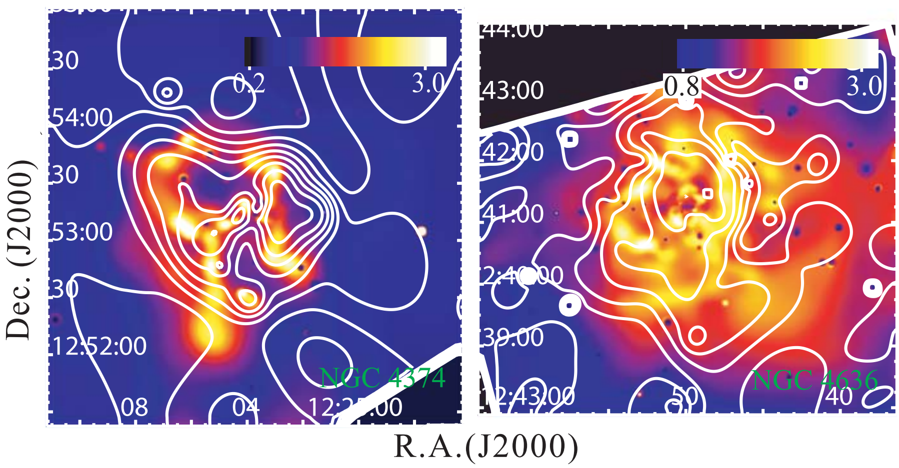

Fig. 2 Distributions of the exposure-corrected and background-subtracted hardness ratio $\mathrm{HR_{FeL}}$, on which the contours of the $\mathrm{HR_{cont}}$ ratio are overlaid. The maps are restricted to the central $2R_{\mathrm{e}}$ regions, and have been adaptively smoothed (Sect. 4.2).

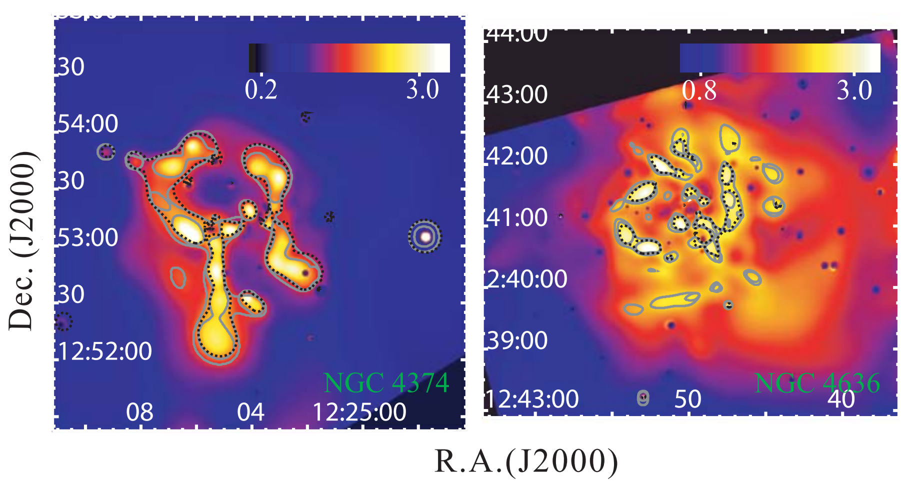

Fig. 3 Same $\mathrm{HR_{FeL}}$ distributions as shown in Fig. 2, on which the wavelet-detected substructures (*solid grey lines*) and substructures in which the mean $\mathrm{HR_{FeL}}$ ratio is higher than that of the surrounding regions by a factor of > 2 (*dotted black lines*) are marked. X-ray point sources are not removed, and they appear as tiny dark spots.

the high-$\mathrm{HR_{FeL}}$ regions may possess high iron metal abundances. In fact, if the large ($>$ a factor of 2) spatial variations in the $\mathrm{HR_{FeL}}$ ratio were not due to significant abundance gradients, but purely due to temperature variations instead, in most cases it is required that the gas temperature of the high-$\mathrm{HR_{FeL}}$ region should be as low as 0.5–0.7 keV, meanwhile the temperature of the vast surrounding regions must reach or be higher than 1.1–1.2 keV. This would result in an average temperature close to 1 keV for the inner regions of the galaxies, which conflicts with the observations; simple simulations with XSPEC show that substructures with such drastic temperature gradients would have been detectable with *Chandra* and *XMM-Newton*.

In a typical high-$\mathrm{HR}_{\mathrm{FeL}}$ region that is marked with dotted black lines in Figure 3, the $\mathrm{HR}_{\mathrm{FeL}}$ ratio ranges from about 2.5 to 3.5–4. A close examination shows that such high $\mathrm{HR}_{\mathrm{FeL}}$ ratios can only appear when the average gas iron abundance is 1.5–2 solar (when kT =0.5–0.8 keV) or even higher (when $kT > 0.8$ keV). Therefore, we conclude that most of the high-$\mathrm{HR}_{\mathrm{FeL}}$ regions are very likely to possess higher abundances than their surrounding regions.

4 DISCUSSION

In order to crosscheck the detections and to avoid possible biases in the à Trous wavelet algorithm, which may be introduced by, e.g., the choice of a specific wavelet kernel, we have applied other multiscale decomposition algorithms, such as the curvelet, ridgelet, and wavelet + ridgelet + curvelet algorithms (see, e.g., Starck et al. 2006 and reference therein for details), and have experimented with different kernels (e.g., the B3-spline kernel). The results confirm our identifications of the high-significance $\mathrm{HR}_{\mathrm{FeL}}$ substructures, as shown in Figure 3.

By examining the spatial distributions of both the resolved X-ray point sources and globular clusters (GCs; Hempel et al. 2003; Maccarone et al. 2003; Richtler et al. 2004; Posson-Brown et al. 2009; Xu et al. 2005; Pierce et al. 2006; see also references in these works), and comparing these distributions with the locations and shapes of the high-$\mathrm{HR}_{\mathrm{FeL}}$ substructures (Fig. 3), whose linear scales ($\sim 1'$; ~ 5 kpc) are much larger than the size of either the *Chandra* ACIS PSF or the uncorrected uncertainties in the aspect solution, we conclude that the high-$\mathrm{HR}_{\mathrm{FeL}}$ substructures are not associated with either the LMXB or globular cluster populations. Therefore, their origins should be related to AGN activity or mergers.

Acknowledgements We thank the Chandra team for making data available via the High Energy Astrophysics Science Archive Research Center (HEASARC) at *http://heasarc.gsfc.nasa.gov*. This work was supported by the National Natural Science Foundation of China (Grant Nos. 10503008, 10673008, 10878001 and 10973010), the Ministry of Science and Technology of China (Grant No. 2009CB824900/2009CB24904), and the Ministry of Education of China (the NCET Program).

References

Carollo, C. M., Franx, M., Illingworth, G. D., & Forbes D. A. 1997, ApJ, 481, 710
de Vaucouleurs, G., de Vaucouleurs, A., Corwin, H. G. Jr., Buta, R. J., Paturel, G., & Fouque, P. 1991, Third Reference Catalog of Bright Galaxies (RC3) (Springer-Verlag: New York)
Dickey, J. M., & Lockman, F. J. 1990, ARA&A, 28, 215
Faber, S. M., Wegner, G., Burstein, D., Davies, R. L., Dressler, A., Lynden-Bell, D., & Terlevich, R. J. 1989, ApJS, 69, 763
Finoguenov, A., & Jones, C. 2001, ApJ, 547, L107
Furusho, T., Yamasaki, N. Y., & Ohashi, T. 2003, ApJ, 596, 181
Gibson, B. K., Sanchez-Blazquez, P., Courty, S., & Kawata, D. 2007, EAS Publications Series, 24, 133
Grevesse, N., & Sauval, A. J. 1998, Space Sci. Rev., 85, 161
Gu, J., Xu, H., Gu, L., An, T., Wang, Y., Zhang, Z., & Wu, X.-P. 2007, ApJ, 659, 275
Hayakawa, A., Furusho, T., Yamasaki, N. Y., Ishida, M., & Ohashi, T. 2004, PASJ, 56, 743
Hayakawa, A., Hoshino, A., Ishida, M., Furusho, T., Yamasaki, N. Y., & Ohashi, T. 2006, PASJ, 58, 695
Hempel, M., Hilker, M., Kissler-Patig, M., Puzia, T. H., Minniti, D., & Goudfrooij, P. 2003, A&A, 405, 487
Johnstone, R. M., Allen, S. W., Fabian, A. C., & Sanders, J. S. 2002, MNRAS, 336, 299
Jones, C., Forman, W., Vikhlinin, A., Markevitch, M., David, L., Warmflash, A., Murray, S., & Nulsen, P. E. J. 2002, ApJ, 567, L115
Kraft, R. P., Forman, W. R., Churazov, E., Laslo, N., Jones, C., Markevitch, M., Murray, S. S., & Vikhlinin, A. 2004, ApJ, 601, 221

Maccarone, T. J., Kundu, A., & Zepf, S. E. 2003, ApJ, 586, 814
Makishima, K., et al. 2001, PASJ, 53, 401
Nagar, N. M., Falcke, H., Wilson, A. S., & Ho, L. C. 2000, ApJ, 542, 186
Ohto, A., Kawano, N., & Fukazawa, Y. 2003, PASJ, 55, 819
O'Sullivan, E., & Ponman, T. J. 2004, MNRAS, 354, 935
O'Sullivan, E., Vrtilek, J. M., & Kempner, J. C. 2005, ApJ, 624, L77
Pierce, M., Bridges, T., Forbes, D. A., Proctor, R., Beasley, M. A., Gebhardt, K., Faifer, F. R., Forte, J. C., Zepf, S. E., Sharples, R., & Hanes, D. A. 2006, MNRAS, 368, 325
Posson-Brown, J., Raychaudhury, S., Forman, W., Donnelly, R. H., & Jones, C. 2009, ApJ, 695, 1094
Prugniel, Ph., & Simien, F. 1996, A&A, 309, 749
Randall, S. W., Sarazin, C. L., & Irwin, J. A. 2004, ApJ, 600, 729
Randall, S. W., Sarazin, C. L., & Irwin, J. A. 2006, ApJ, 636, 200
Ravindranath, S., Ho, L. C., Peng, C. Y., Filippenko, A. V., & Sargent, W. L. W. 2001, AJ, 122, 653
Richtler, T., Dirsch, B., Gebhardt, K., Geisler, D., Hilker, M., Alonso, M. V., Forte, J. C., Grebel, E. K., Infante, L., Larsen, S., Minniti, D., & Rejkuba, M. 2004, AJ, 127, 2094
Sanders, J. S., Fabian, A. C., & Dunn, R. J. H. 2005, MNRAS, 360, 133
Shensa, M. J. 1992, IEEE Transactions on Signal Processing, 40(10), 2464
Starck, J.-L., Moudden, Y., Abrial, P., & Nguyen, M. 2006, A&A, 446, 1191
Tonry, J. L., Dressler, A., Blakeslee, J. P., Ajhar, E. A., Fletcher, A. B., Luppino, G. A., Metzger, M. R., & Moore, C. B. 2001, ApJ, 546, 681
Xilouris, E. M., Madden, S. C., Galliano, F., Vigroux, L., & Sauvage, M. 2004, A&A, 416, 41
Xu, Y., Xu, H., Zhang, Z., Kundu, A., Wang, Y., & Wu, X. 2005, ApJ, 631, 809